JOURNAL OF PETROLOGY | VOLUME 55 | NUMBER 3 | PAGES 671–684 | 2014 | doi:10.1093/petrology/egt079

TECHNICAL NOTE
Monitoring the Magmas Fuelling Volcanic Eruptions in Near-real-time Using X-ray Micro-computed Tomography

M. J. PANKHURST[1]*, K. J. DOBSON[2,3], D. J. MORGAN[1], S. C. LOUGHLIN[4], TH. THORDARSON[5], P. D. LEE[2,3] AND L. COURTOIS[2,3]

[1]INSTITUTE OF GEOPHYSICS AND TECTONICS, SCHOOL OF EARTH AND ENVIRONMENT, UNIVERSITY OF LEEDS, LEEDS LS2 9JT, UK

[2]MANCHESTER X-RAY IMAGING FACILITY, SCHOOL OF MATERIALS, THE UNIVERSITY OF MANCHESTER, OXFORD ROAD, MANCHESTER M13 9PL, UK

[3]RESEARCH COMPLEX AT HARWELL, RUTHERFORD APPLETON LABORATORIES, DIDCOT OX11 0FA, UK

[4]BRITISH GEOLOGICAL SURVEY, EDINBURGH, EH9 3LA, UK

[5]INSTITUTE OF EARTH SCIENCE, UNIVERSITY OF ICELAND, SÆMUNDARGÖTU 2, 101 REYKJAVÍK, ICELAND

RECEIVED SEPTEMBER 23, 2013; ACCEPTED DECEMBER 17, 2013
ADVANCE ACCESS PUBLICATION JANUARY 24, 2014

A novel application of X-ray micro-computed tomography is described, which can be used to rapidly characterize chemical populations of natural olivine crystals in erupted basalts. This technique can be deployed during volcanic crises to directly track changes in magma components of an erupting system in near-real-time. Such changes are fundamental in controlling eruption style, duration and intensity. We demonstrate a method that can generate data from hundreds of crystals within hours, which allows time-series petrological data to be recorded and interpreted alongside various complementary monitoring techniques (e.g. seismicity, ground deformation). Our direct-detection will allow greater understanding of the dynamics of sub-volcanic magma plumbing systems, and can provide important insights into how an eruption may evolve. The same technique can also be used to generate rich baseline datasets from eruption sequences in the geological record in a more efficient manner than conventional methods allow.

KEY WORDS: *X-ray micro-computed tomography; olivine composition; volcanic eruption monitoring*

INTRODUCTION

Volcanic eruptions are often triggered, sustained, or terminated by changes in magmatic conditions that affect the physical behaviour of the magma; these include temperature (T), pressure (P), melt composition including volatile (e.g. H_2O) content (X), and consequent gas and mineral phase stability (Bardintzeff & Bonin, 1987; Cashman, 1992; Papale *et al.*, 1998; Pinkerton *et al.*, 2002; Rutherford & Devine, 2003; Izbekov *et al.*, 2004). Mixing between different magma batches is frequently implicated as the cause of such changes, with a common scenario being a new magma pulse entering the sub-volcanic plumbing system (Sparks *et al.*, 1977; Huppert *et al.*, 1982; Sigmundsson *et al.*, 2010). Developing the capability to detect such changes, understand their influence, and ultimately forecast future eruptive events with high temporal resolution is a continuing goal of volcanologists (Aiuppa *et al.*, 2002; Sparks *et al.*, 2012), owing to the enormous capacity for volcanic

*Corresponding author. E-mail: m.j.pankhurst@leeds.ac.uk

eruptions to cause both local (Tanguy, 1994) and global natural disasters (Self, 2006).

In addition to predicting the beginning of an eruption, other important questions are: 'How large, for how long a duration, and therefore how hazardous could a new eruption become?' These forecasts are critical to effective planning and crisis management. For instance, in an Icelandic setting, an initial small fissure eruption may have the potential to evolve into a small magnitude 2010 Eyjafjallajökull-style event (Stevenson *et al.*, 2012), or a large magnitude eruption such as the AD 1783–1784 Laki event (Thordarson & Self, 2003). The frequency of explosive eruptions within Iceland and in other volcanic settings around the world in historical times, and the large variability in scale they exhibit (Thordarson & Larsen, 2007), emphasizes the importance of these questions.

The role of igneous petrology in understanding volcanic risk

Igneous petrology provides insights into the conditions of magma generation and storage and the drivers of volcanic processes. The saturation of phenocryst minerals during the evolution of a magma is controlled by variations in P, T and X of the host melt through time (Wilson, 1989). Cooling magmatic systems typically evolve from mafic (Mg-rich) to more felsic (SiO_2-rich) compositions in response to fractionation of mafic minerals, and the Mg# [$100 \times Mg/(Mg + Fe)$] of the residual liquid decreases with time (Villiger *et al.*, 2004). Important physicochemical changes in the magma occur simultaneously with this differentiation, including increases in volatile concentrations and changes in crystal type, abundance and chemistry. Concomitant changes in magma viscosity also occur (Giordano *et al.*, 2008). The erupted volcanic products may thus preserve a record of the changing magmatic conditions in P–T–X space with time in the chemistry of the phenocryst minerals (Fram & Lesher, 1997; Thy *et al.*, 2006).

Interaction between batches of magma with different intensive parameters (including P, T, X, crystal and gas bubble content) is a common process (Streck, 2008) that can add further complexity to the overall magmatic system as it evolves. Because eruption dynamics are largely controlled by the physicochemical state of the magma (Papale *et al.*, 1998), monitoring such interaction is of considerable importance. Directly observable consequences of significant magmatic change induced by mixing processes include changes in crystal populations and in crystal chemistry (Sigmarsson *et al.*, 2011).

Magmatic provenance and change indicated by olivine crystal chemical populations

The composition of olivine is particularly sensitive to changes in magma composition, P, T and oxygen fugacity (Putirka, 2008; Matzen *et al.*, 2011). In basalt-dominated terrains such as Iceland, the olivine chemical population(s) in the erupted basalts can be used to identify the likely magma source regions (e.g. deep versus shallow crust) and thus differentiate between a large, deep-seated rift event or a small, shallow, remobilized magma event (Sigmarsson *et al.*, 2011). As such, olivine chemical populations could provide an indication of the eventual scale and progression of a new eruption. Furthermore, changing crystal chemical populations throughout an eruption sequence may indicate changing magmatic conditions, potentially owing to changes in the relative volumes of interacting magma batches each contributing the signature of their crystal load to the volcanic products.

Olivine is primarily a solid-solution between forsterite (Mg_2SiO_4: denoted as Fo_{100} or Mg# = 100) and fayalite (Fe_2SiO_4: Fo_0, Mg# = 0), and the Fe–Mg mineral–melt partitioning is well understood (Roeder & Emslie, 1970). Therefore the Mg# of olivine precipitating from a melt represents a proxy for the stage of differentiation of the equilibrium melt. Hence olivine Mg# populations can provide important constraints upon local melt conditions and larger-scale magmatic processes (Thomson & Maclennan, 2013).

Whereas the rim of a growing magmatic olivine crystal reflects the composition of the adjacent melt, its interior provides a record of earlier conditions specific to that crystal. A number of processes contribute to the crystal population in a magma. Phenocrysts grow in the magma containing them, antecrysts are earlier precipitates from a discrete but kindred magma/cumulate mush, and xenocrysts are plucked from unrelated wall-rocks or cumulate mush (Hildreth & Wilson, 2007; Streck, 2008). Natural magmatic systems can therefore be highly complex, and involve interaction between multiple magma batches, each bringing their distinct crystal population and history to the mix.

This rich complexity can provide powerful insights into magmatic systems if the contributions from individual components can be identified (Kahl *et al.*, 2011). If sufficient numbers of crystals can be analysed to produce statistically robust datasets (Thomson & Maclennan, 2013), changes to magmas and/or contributions from different magma batches can be tracked in the erupted crystals throughout an eruption sequence. In this manner, monitoring relative changes to crystal chemical populations in near-real-time during a volcanic eruption would represent a major advance.

THE PROBLEM

Conventional chemical analysis of crystals requires time intensive preparation. Each mount may take several hours to prepare (to fully set the resin, which is then ground to expose the grains, and polished to a high-quality finish before being carbon coated). Crystals can be analysed

only one at a time by electron-probe micro-analysis (EPMA). A few minutes per analytical spot are sufficient to produce quantitative data for major elements and a small number of trace elements. Optimized EPMA and fully quantified energy-dispersive X-ray spectroscopy system set-ups may increase sample throughput, yet necessarily sacrifice precision and the number of elements analysed. Even with an optimized system involving electron beam analysis the sample material still needs to be mounted in resin, polished and carbon coated. Although direct calls have recently been made to monitor eruptive material (Sigmundsson & Hoskuldsson, 2010), and despite the long-recognized advantages of applying petrological data to volcano monitoring (Devine *et al.*, 1998*a*, 1998*b*), rapid high-volume throughput in a time-sensitive situation (i.e. a current eruption) using standard methods remains problematic.

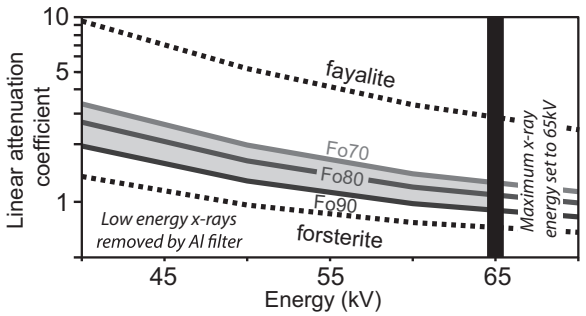

Fig. 1. The dependence of linear attenuation coefficient on X-ray energy for olivine. The linear attenuation coefficient increases with decreasing Mg#. Scanning at lower energies, where the contrast in attenuation coefficient is greatest, results in a wider dynamic range in the reconstructed 3D images. The attenuation coefficient curves for olivine compositions bracketing our samples are shown. The Nikon XTH 225ST XMT system was run with a polychromatic X-ray beam with a maximum energy of 65 kV, and a peak flux at ~40 kV.

OUR APPROACH

To overcome the above impediment we turn our attention to a far faster method, X-ray micro-computed tomography (XMT; Stock, 1999), and use it to analyse large numbers of entire crystals simultaneously. XMT is a non-destructive density-sensitive imaging method that allows density contrasts to be mapped in three dimensions. Samples are rotated in an X-ray beam while a high-resolution scintillator fronted CCD detector collects images (projections) at different angles. The projections are then 'reconstructed' using numerical algorithms to produce a full 3D render of the internal structure of the object (Stock, 1999). Modern laboratory and synchrotron imaging systems can acquire data in as little as a few seconds, at a voxel (the 3D equivalent of a pixel) resolution of <2 μm. Applications to geological materials prior to our study have focused upon identifying different phases and minerals, and investigating their relationships in static or dynamic three dimensions (Cnudde & Boone, 2013). Greyscale values can be compared between scans if secondary standards are used that encompass the X-ray attenuation coefficient of the material of interest; these allow correction for variations in absolute greyscale value that can be caused by fluctuations in X-ray beam current and flux (owing to filament age, instrument behaviour, etc.).

The X-ray linear attenuation coefficient of forsterite and fayalite differs significantly under typical laboratory scan conditions (40–60 kV, Fig. 1). Here we investigate (1) whether this difference in attenuation coefficient is sufficient for useful discrimination between olivine crystal compositions, (2) whether observed differences can be confidently mapped to measured composition differences, and (3) how quickly these data can be generated. We have simulated the throughput of samples in a time-sensitive situation to test how quickly volcano observatories might be able to produce and interpret data during a volcanic crisis. We used a sample of tephra erupted from the 2010 Fimmvörðuháls flank eruption prior to the Eyjafjallajökull summit eruption in the Eastern Volcanic Zone (EVZ) of Iceland, as similar material is most likely to be sequentially sampled during future eruptions.

METHOD

The tephra sample was manually crushed using a steel rolling pin and an aluminum bash-plate before being sieved. One hundred grains containing an olivine crystal were picked directly from the 0·5–2·0 mm fraction (grains containing whole, intact crystals were preferred), loaded into ~2·0 cm lengths of plastic straw (internal diameter = 4 mm), and capped with pre-prepared resin discs. Three grains containing plagioclase crystals of a similar size to the olivine were added as a control. This experimental charge was then scanned using a Nikon XTH 225ST XMT system at the University of Manchester at a maximum energy of 65 kV using a 1·0 Al filter to minimize beam hardening. This system has a standard static X-ray source and detector (which resolves 2000 × 2000 pixels); thus with decreasing distance between the sample and the source, the greater the absolute resolution. The sample rotates around a vertical axis while projections are taken about 360°. Using more projections decreases the number and intensity of reconstruction artefacts, at the expense of time. We found that the balance between data quality and speed of acquisition was optimal at 2000 projections (every 0·18°) per scan.

The data were reconstructed using proprietary software to produce a 3D volume containing all 103 grains with a voxel resolution of ~2·5 μm. Digital image processing techniques were used to isolate each olivine crystal using *Aviso*® and *Fiji*. This involved using pre-existing and freely available plugins to 'train' the software to distinguish

olivine from plagioclase, glass and air. Once identified, each crystal in the olivine fraction was digitally eroded inwards from the rim by the equivalent of ~15 μm to ensure only the core of the crystals remained. This avoided the sampling of heterogeneous rims, with the attendant potential for error, during subsequent analysis. The average greyscale value of a 'spot' of identical size (25 μm radius) was then calculated for each crystal core, excluding obvious inclusions, cracks or zoning. This last step was performed manually to ensure a robust dataset with which to compare against future, more sophisticated/automated, image processing methods, and to validate against conventional methods whereby analysis positions are chosen manually.

Standard EPMA techniques were used to measure the compositions of 100 olivine crystal cores from a second split of the same sample using a JEOL 8230 electron microprobe at the University of Leeds (see Appendix for full analytical conditions).

RESULTS

The entire XMT method took <2·5 h (see Fig. 2). Total sample preparation time was ~20 min. The scanning and reconstruction steps (image acquisition) were performed in ~30 min each. Image processing (including manual selection) took ~60 min.

In the studied sample olivine, plagioclase, glass and air that make up the 3D volume were easily distinguished based on habit, texture and greyscale value. The plagioclase (used as a control) was identified by its habit, texture and (low) greyscale value. Thirteen olivine crystals were discarded owing to cracks or inclusions. The reconstructed volume contains olivine crystals with a range of greyscale values, and often reveals zoning around homogeneous cores (Fig. 2). Thus we can demonstrate that XMT is capable of resolving even subtle changes in Mg# in natural olivine crystals.

A frequency diagram of the greyscale values was constructed from both the XMT-spot ($n = 87$) and EPMA-spot ($n = 100$) datasets using nine bins (~10% of each n) of equal range (Fig. 3). A distinct pattern of greyscale value population frequency is observed, and is matched by the compositional variations determined by EPMA (Fig. 3). Subtle differences between the two datasets are due to a combination of the non-linear energy dependence of the X-ray attenuation coefficient, which is more pronounced at high Mg# (see Fig. 1), and the use of two sets of olivine crystals from the same sample. The EPMA data are reported in Table A1 and the XMT data in Table A2. Rank-order and linear-array plots of the XMT and EPMA data are provided along with the raw data in the Appendix (Fig. A1 and Table A3, respectively). The range of greyscale values in each XMT data bin is provided in Table A4.

Identification and quantification of chemical population(s) of macrocryst phases is an important step in unravelling the petrogenesis of igneous rocks, and is a key result of our study. Figure 3 demonstrates the existence of a dominant olivine chemical population of ~Fo_{80} in the studied sample. Two sub-dominant populations are also evident, at ~Fo_{76} and ~Fo_{84}, which indicates disequilibria of the system at the time of eruption. Taken at face value, these three peaks may demonstrate the presence of a number of magmatic components in the erupted sample. These have arguably mixed shortly before eruption, as olivine not in equilibrium with the host melt will be eventually resorbed.

We find that the XMT method is far faster than standard analysis techniques. It has the ability to accurately distinguish chemical populations, as confirmed by the EPMA data. The use of secondary standards that bracket and intersperse the X-ray attenuation coefficient range of olivine should allow fully comparable data between scans. We conclude that XMT holds great potential to be used as a high-throughput, rapid and accurate method for characterizing crystal chemical populations, which opens up a powerful new approach to volcanic eruption monitoring, and will allow the generation of rich baseline datasets.

FUTURE APPLICATIONS

To make best use of olivine XMT data in a time-critical scenario such as a volcanic eruption, the absolute chemical composition and zonation of olivine crystals must be assessed soon after eruption. Optimized EPMA techniques on polished crystal mounts produce high-precision data, but they are time intensive, destructive and limited to 1D and 2D profiles. With appropriate calibration and use of secondary standards, our XMT technique could approach the precision and accuracy of current EPMA methods in terms of major element chemical composition, and open further avenues for its application in volcanic eruption monitoring.

Recently developed understanding of solid-state Fe–Mg diffusion between zones of different Mg# within olivine has effectively turned zonation profiles in each crystal into a stopwatch for magmatic processes (Costa & Dungan, 2005; Morgan & Blake, 2006; Dohmen & Chakraborty, 2007; Costa *et al.*, 2008). Characterization of the zoning of single olivine crystals and of crystal populations in eruption sequences can enhance our understanding of the evolution of sub-volcanic magma plumbing systems through time, on a range of scales (Kahl *et al.*, 2011, 2013). With large enough olivine composition datasets, a detailed picture of the magmatic processes fuelling basaltic eruptions through time can be obtained, and compared with seismic unrest and ground deformation signals. This information can aid interpretation of geophysical unrest signals during pre- and syn-eruption events in the future.

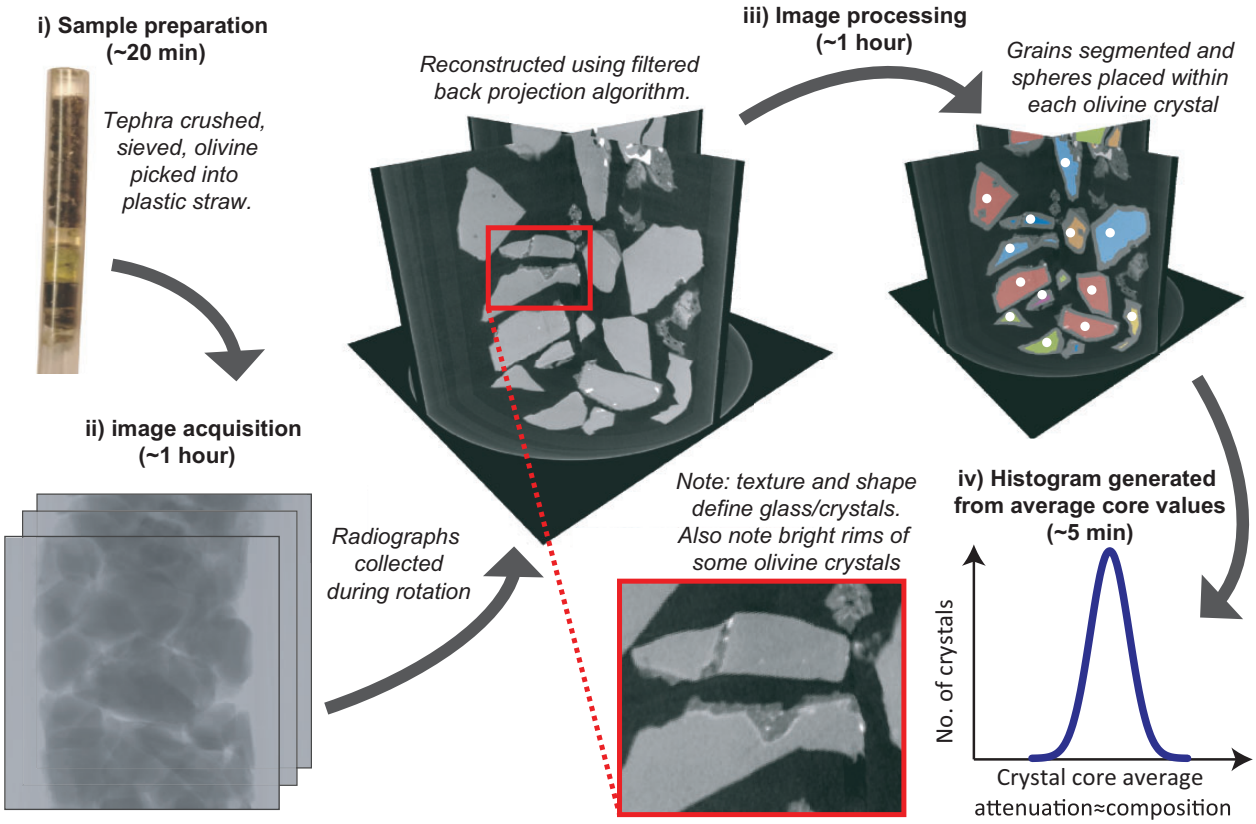

Fig. 2. XMT workflow for determining olivine crystal composition populations within 2·5 h of sample receipt. Crystals are easily distinguished on the basis of texture and shape. Low-density olivine (high Mg#) appears darker than higher density olivine (low Mg#). Refinement of the experimental setup may allow faster scanning, and trainable algorithm-based analysis may decrease this workflow time further without sacrificing data quality. Volumes for greyscale value averaging were selected to simulate an EPMA spot, and were placed within the crystal cores, shown schematically as white spots.

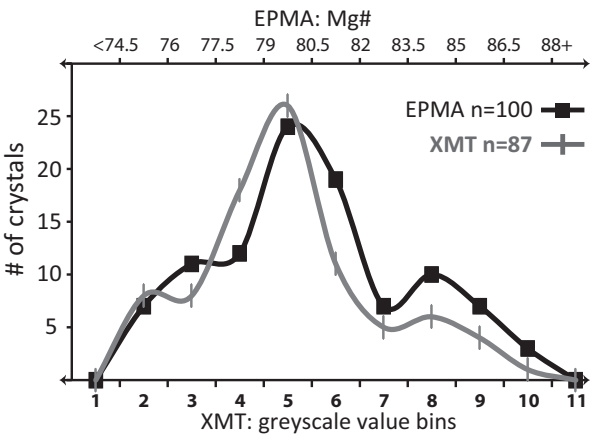

Fig. 3. Comparison between XMT greyscale value data and EPMA (Mg#) data from olivine crystals in tephra erupted during the 2010 Fimmvörðuháls eruption. The XMT data were generated using the XMT workflow described in the text and summarized in Fig. 2. A single EPMA spot was analysed in each crystal core (see the Appendix for analytical details). The values in each dataset were divided into nine bins of equal range. The peaks in each population correlate well.

Within basaltic systems such as the active EVZ of Iceland olivine is almost ubiquitous, and records a variety of origins (Passmore *et al.*, 2012). Olivine in these rocks is commonly chemically zoned: generally a homogeneous core is fringed by comparatively narrow zones of different olivine composition (Thomson & Maclennan, 2013). Volcanic systems such as these represent prime candidates for XMT-based generation of rich datasets of olivine composition populations and magmatic timescales through eruption sequences. Furthermore, integrating crystal size distribution (CSD) and modal abundance data with our rapid composition determination approach could be a powerful tool in understanding magma dynamics and, by extension, understanding crystal–melt relationships. XMT can be used to measure CSDs (Jerram *et al.*, 2009), and each crystal can be assigned a unique digital label, allowing large populations of crystals to be characterized by size and composition.

In the short term, linking olivine chemical population changes with well-resolved eruption phenomenology (duration, intensity, style) in a forensic manner and merging

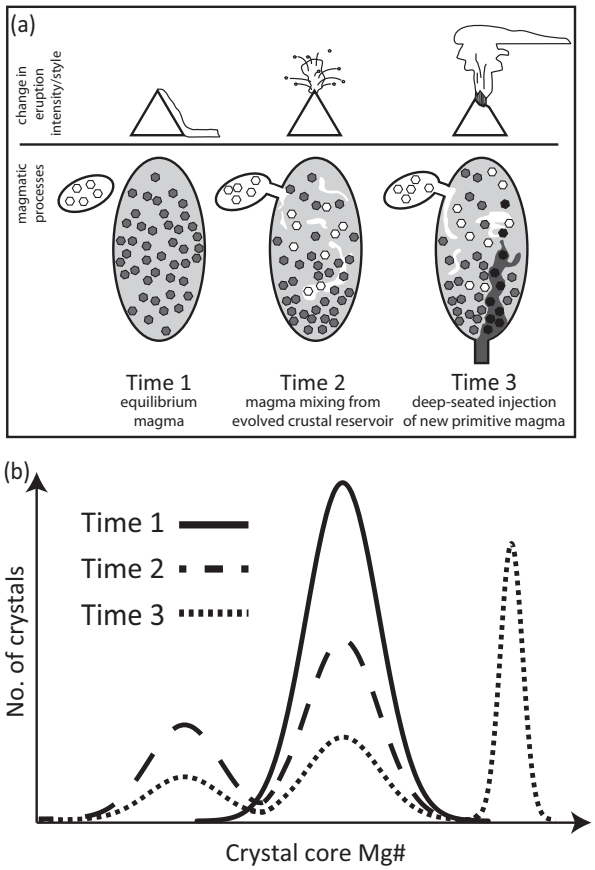

Fig. 4. (a) Schematic illustration of hypothetical volcano behaviour (observed in real-time) to illustrate the response to major changes within the magma plumbing system during a protracted eruption. Light shades indicate silicic melts and Fe-rich olivine compositions (i.e. shallow equilibrated, evolved magma), whereas dark shades indicate Mg-rich compositions (i.e. deeply equilibrated, primitive magma). (b) Olivine crystal chemical population frequency curves stacked through time, corresponding to the eruption sequences shown in (a). Such data could be generated from erupted material using a workflow similar to that described in this study, allowing insight into magmatic processes at a high temporal resolution. These data may be compared with the record of event chronology during volcanic eruptions to identify possible correlations with seismic data, ground deformation changes and gas monitoring data in near-real-time. Similar plots based on data from past eruptions may be used as empirical guides to future eruptive events.

this with geophysical datasets (Kahl *et al.*, 2013) holds potential to discover important patterns that could be recognized during a future eruption. There is an urgent need for well-documented analysis of past eruptive events, as they hold the key to well-constrained pattern recognition. These patterns could be used as empirical lead-indicators of eruptive change, duration and cessation, which are key issues during a volcanic crisis (see Fig. 4). Building this knowledge could be accelerated by using the high-throughput XMT method described here.

Although many hazardous volcanoes erupt olivine-phyric basalts, many do not. The XMT method is not limited to olivine, for the principles of variable X-ray attenuation coefficient as a proxy for variable composition also applies to many other phenocryst minerals and glasses. Those with solid-solutions whose end-member compositions represent a large density contrast are particularly suited to this method, such as enstatite–ferrosilite and anorthite–albite. By applying a similar method to other minerals such as orthopyroxene and plagioclase, the XMT technique will be of use in a greater number of volcanic settings. In addition, XMT techniques are not limited to the study of volcanic samples; 3D applications for observing compositional variations in intrusive magmatic rocks and even mantle rocks (xenoliths; orogenic peridotites) could hold great potential. Since XMT generates high quality 3D textural data, it holds great potential for use as a provider of specific and timely particle shape, size and density information as inputs to next generation ash dispersion models.

ACKNOWLEDGEMENTS

The authors wish to thank Dennis Geist, Bruce Marsh and Kate Saunders for their thoughtful reviews of this paper, and Marjorie Wilson and Alastair Lumsden for their editorial roles. M.J.P., D.J.M., Th.T. and S.C.L. are supported by NERC grant NE/J024554/1. K.J.D., L.C. and P.D.L. wish to acknowledge EPSRC grant EP/I02249X/1, which supports the Manchester X-ray Imaging Facility, and the Research Complex at Harwell. The Faversham is thanked for providing plastic drinking straws for our experimental apparatus. Harri Wyn Williams and Martin Coldwell are thanked for providing sample preparation advice and assistance. The Natural History Museum, London, UK, is thanked for providing mineral specimens used in the proof of concept stage of this work.

REFERENCES

Aiuppa, A., Federico, C., Paonita, A., Pecoraino, G. & Valenza, M. (2002). S, Cl and F degassing as an indicator of volcanic dynamics: The 2001 eruption of Mount Etna. *Geophysical Research Letters* **29(11)**, 54-1–54-4.

Bardintzeff, J.-M. & Bonin, B. (1987). The amphibole effect: A possible mechanism for triggering explosive eruptions. *Journal of Volcanology and Geothermal Research* **33(4)**, 255–262.

Cashman, K. (1992). Groundmass crystallization of Mount St. Helens dacite, 1980–1986: a tool for interpreting shallow magmatic processes. *Contributions to Mineralogy and Petrology* **109(4)**, 431–449.

Cnudde, V. & Boone, M. N. (2013). High-resolution X-ray computed tomography in geosciences: A review of the current technology and applications. *Earth-Science Reviews* **123**, 1–17.

Costa, F. & Dungan, M. (2005). Short time scales of magmatic assimilation from diffusion modeling of multiple elements in olivine. *Geology* **33(10)**, 837–840.

Costa, F., Dohmen, R. & Chakraborty, S. (2008). Time scales of magmatic processes from modeling the zoning patterns of crystals. In: Putirka, K. D. & Tepley, F. J., III (eds) *Minerals, Inclusions and Volcanic Processes. Mineralogical Society of America and Geochemical Society, Reviews in Mineralogy and Geochemistry* **69**, 545–594.

Devine, J. D., Murphy, M. D., Rutherford, M. J., Barclay, J., Sparks, R. S. J., Carroll, M. R., Young, S. R. & Gardner, I. E. (1998*a*). Petrologic evidence for pre-eruptive pressure–temperature conditions, and recent reheating, of andesitic magma erupting at the Soufrière Hills Volcano, Montserrat, W.I. *Geophysical Research Letters* **25(19)**, 3669–3672.

Devine, J. D., Rutherford, M. J. & Gardner, J. E. (1998*b*). Petrologic determination of ascent rates for the 1995–1997 Soufrière Hills Volcano andesitic magma. *Geophysical Research Letters* **25(19)**, 3673–3676.

Dohmen, R. & Chakraborty, S. (2007). Fe–Mg diffusion in olivine II: Point defect chemistry, change of diffusion mechanisms and a model for calculation of diffusion coefficients in natural olivine. *Physics and Chemistry of Minerals* **34(6)**, 409–430.

Fram, M. S. & Lesher, C. E. (1997). Generation and polybaric differentiation of East Greenland Early Tertiary flood basalts. *Journal of Petrology* **38(2)**, 231–275.

Giordano, D., Russell, J. K. & Dingwell, D. B. (2008). Viscosity of magmatic liquids: A model. *Earth and Planetary Science Letters* **271(1–4)**, 123–134.

Hildreth, W. & Wilson, C. J. N. (2007). Compositional zoning of the Bishop Tuff. *Journal of Petrology* **48(5)**, 951–999.

Huppert, H. E., Sparks, R. S. J. & Turner, J. S. (1982). Effects of volatiles on mixing in calc-alkaline magma systems. *Nature* **297(5867)**, 554–557.

Izbekov, P. E., Eichelberger, J. C. & Ivanov, B. V. (2004). The 1996 eruption of Karymsky Volcano, Kamchatka: historical record of basaltic replenishment of an andesite reservoir. *Journal of Petrology* **45(11)**, 2325–2345.

Jerram, D. A., Mock, A., Davis, G. R., Field, M. & Brown, R. J. (2009). 3D crystal size distributions: A case study on quantifying olivine populations in kimberlites. *Lithos* **112(Supplement 1)**, 223–235.

Kahl, M., Chakraborty, S., Costa, F. & Pompilio, M. (2011). Dynamic plumbing system beneath volcanoes revealed by kinetic modeling, and the connection to monitoring data: An example from Mt. Etna. *Earth and Planetary Science Letters* **308(1–2)**, 11–22.

Kahl, M., Chakraborty, S., Costa, F., Pompilio, M., Liuzzo, M. & Viccaro, M. (2013). Compositionally zoned crystals and real-time degassing data reveal changes in magma transfer dynamics during the 2006 summit eruptive episodes of Mt. Etna. *Bulletin of Volcanology* **75(2)**, 1–14.

Matzen, A. K., Baker, M. B., Beckett, J. R. & Stolper, E. M. (2011). Fe–Mg partitioning between olivine and high-magnesian melts and the nature of Hawaiian parental liquids. *Journal of Petrology* **52(7–8)**, 1243–1263.

Morgan, D. J. & Blake, S. (2006). Magmatic residence times of zoned phenocrysts: Introduction and application of the binary element diffusion modelling (BEDM) technique. *Contributions to Mineralogy and Petrology* **151(1)**, 58–70.

Papale, P., Neri, A. & Macedonio, G. (1998). The role of magma composition and water content in explosive eruptions: 1. Conduit ascent dynamics. *Journal of Volcanology and Geothermal Research* **87(1–4)**, 75–93.

Passmore, E., Maclennan, J., Fitton, G. & Thordarson, T. (2012). Mush disaggregation in basaltic magma chambers: evidence from the AD 1783 Laki eruption. *Journal of Petrology* **53(12)**, 2593–2623.

Pinkerton, H., Wilson, L. & MacDonald, R. (2002). The transport and eruption of magma from volcanoes: A review. *Contemporary Physics* **43(3)**, 197–210.

Putirka, K. D. (2008). Thermometers and barometers for volcanic systems. In: Putirka, K. D. & Tepley, F. J., III (eds) *Minerals, Inclusions and Volcanic Processes. Mineralogical Society of America and Geochemical Society, Reviews in Mineralogy and Geochemistry* **69**, 61–120.

Roeder, P. L. & Emslie, R. F. (1970). Olivine–liquid equilibrium. *Contributions to Mineralogy and Petrology* **29(4)**, 275–289.

Rutherford, M. J. & Devine, J. D. (2003). Magmatic conditions and magma ascent as indicated by hornblende phase equilibria and reactions in the 1995–2002 Soufrière Hills magma. *Journal of Petrology* **44(8)**, 1433–1454.

Self, S. (2006). The effects and consequences of very large explosive volcanic eruptions. *Philosophical Transactions of the Royal Society of London, Series A* **364(1845)**, 2073–2097.

Sigmarsson, O., Vlastelic, I., Andreasen, R., Bindeman, I., Devidal, J. L., Moune, S., Keiding, J. K., Larsen, G., Höskuldsson, A. & Thordarson, T. H. (2011). Remobilization of silicic intrusion by mafic magmas during the 2010 Eyjafjallajökull eruption. *Solid Earth* **2(2)**, 271–281.

Sigmundsson, F. & Hoskuldsson, A. (2010). Develop instruments to monitor volcanic ash fallout. *Nature* **466(7302)**, 28–28.

Sigmundsson, F., Hreinsdóttir, S., Hooper, A., Árnadóttir, T., Pedersen, R., Roberts, M. J., Óskarsson, N., Auriac, A., Decriem, J., Einarsson, P., Geirsson, H., Hensch, M., Ófeigsson, B. G., Sturkell, E., Sveinbjörnsson, H. & Feigl, K. L. (2010). Intrusion triggering of the 2010 Eyjafjallajökull explosive eruption. *Nature* **468(7322)**, 426–432.

Sparks, S. R. J., Sigurdsson, H. & Wilson, L. (1977). Magma mixing: a mechanism for triggering acid explosive eruptions. *Nature* **267(5609)**, 315–318.

Sparks, R. S. J., Biggs, J. & Neuberg, J. W. (2012). Monitoring volcanoes. *Science* **335**, 1310–1311.

Stevenson, J. A., Loughlin, S., Rae, C., Thordarson, T., Milodowski, A. E., Gilbert, J. S., Harangi, S., Lukács, R., Hjgaard, B., Árting, U., Pyne-O'Donnell, S., MacLeod, A., Whitney, B. & Cassidy, M. (2012). Distal deposition of tephra from the Eyjafjallajökull 2010 summit eruption. *Journal of Geophysical Research B: Solid Earth* **117(B9)**, B00C10, doi:10.1029/2011JB008904.

Stock, S. R. (1999). X-ray microtomography of materials. *International Materials Reviews* **44(4)**, 141–164.

Streck, M. J. (2008). Mineral textures and zoning as evidence for open system processes. In: Putirka, K. D. & Tepley, F. J., III (eds) *Minerals, Inclusions and Volcanic Processes. Mineralogical Society of America and Geochemical Society, Reviews in Mineralogy and Geochemistry* **69**, 595–622.

Tanguy, J. C. (1994). The 1902–1905 eruptions of Montagne Pelée, Martinique: anatomy and retrospection. *Journal of Volcanology and Geothermal Research* **60(2)**, 87–107.

Thomson, A. & Maclennan, J. (2013). The distribution of olivine compositions in Icelandic basalts and picrites. *Journal of Petrology* **54(4)**, 745–768.

Thordarson, T. & Larsen, G. (2007). Volcanism in Iceland in historical time: Volcano types, eruption styles and eruptive history. *Journal of Geodynamics* **43(1)**, 118–152.

Thordarson, T. & Self, S. (2003). Atmospheric and environmental effects of the 1783–1784 Laki eruption: A review and reassessment. *Journal of Geophysical Research D: Atmospheres* **108(1)**, AAC7-1–AAC7-29.

Thy, P., Lesher, C. E., Nielsen, T. F. D. & Brooks, C. K. (2006). Experimental constraints on the Skaergaard liquid line of descent. *Lithos* **92(1–2)**, 154–180.

Villiger, S., Ulmer, P., Müntener, O. & Thompson, A. B. (2004). The liquid line of descent of anhydrous, mantle-derived, tholeiitic liquids by fractional and equilibrium crystallization—an experimental study at 1·0 GPa. *Journal of Petrology* **45(12)**, 2369–2388.

Wilson, M. (1989). *Igneous Petrogenesis*. Chapman & Hall.

APPENDIX

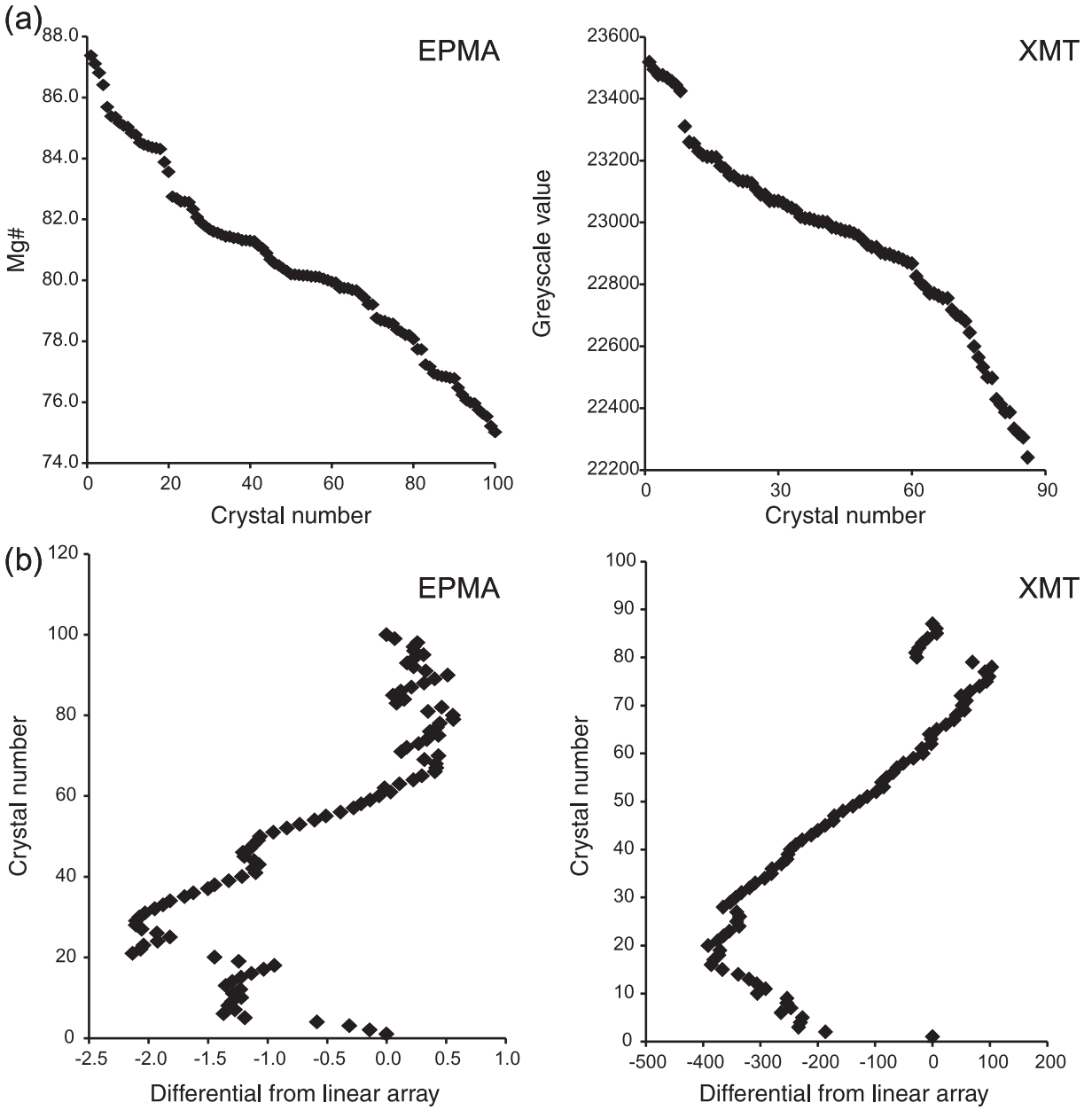

Fig. A1. Comparison between olivine chemical population data generated by EPMA and XMT from two splits of the same sample of Fimmvörðuháls tephra. (a) Decreasing rank-order plots of 100 EPMA Mg# spots (one in each crystal core) with increasing Mg#, and 87 XMT greyscale value spots (averaged 16-bit greyscale value) with increasing greyscale value. (b) Linear-array plots of the same EPMA and XMT data. The differential captures the degree to which each data point (each crystal) departs from a straight line between the highest and lowest value on the corresponding rank-order plot, so that comparisons are easier to make visually. It should be noted that higher greyscale values denote brighter voxels = lower Mg#. As such, the XMT linear-array order is inverted to allow comparison against Mg#.

Table A1: Olivine core compositions measured by EPMA

Crystal	Oxide (wt %)									Mg#
	SiO_2	TiO_2	Al_2O_3	FeO	MnO	MgO	CaO	NiO	Total	
FMVDCT__A1a	40·04	0·02	0·05	12·18	0·15	46·71	0·24	0·38	99·77	87·10
FMVDCT__B1	39·76	0·01	0·03	14·56	0·20	44·68	0·23	0·36	99·84	84·37
FMVDCT__C1	38·47	0·02	0·05	21·32	0·31	38·95	0·29	0·14	99·55	76·25
FMVDCT__D1	38·81	0·02	0·04	19·73	0·31	40·61	0·28	0·07	99·87	78·31
FMVDCT__E1	39·43	0·01	0·04	16·59	0·26	42·76	0·24	0·25	99·58	81·90
FMVDCT__F1	38·62	0·04	0·02	20·95	0·31	39·45	0·30	0·14	99·82	76·79
FMVDCT__G1	38·97	0·03	0·03	18·78	0·29	41·32	0·27	0·20	99·89	79·43
FMVDCT__H1	38·80	0·02	0·04	19·42	0·27	40·60	0·30	0·16	99·61	78·61
FMVDCT__I1	38·56	0·02	0·04	20·54	0·33	39·71	0·28	0·10	99·58	77·23
FMVDCT__J1	39·67	0·02	0·05	15·26	0·24	44·18	0·27	0·26	99·93	83·56
FMVDCT__A2	39·40	0·01	0·04	16·08	0·22	43·36	0·24	0·26	99·62	82·59
FMVDCT__B2	38·79	0·03	0·03	19·34	0·29	40·85	0·28	0·12	99·73	78·77
FMVDCT__C2	39·82	0·01	0·05	14·17	0·21	45·12	0·23	0·29	99·90	84·83
FMVDCT__D2	39·77	0·02	0·04	13·87	0·18	45·27	0·26	0·34	99·74	85·17
FMVDCT__E2	38·52	0·03	0·03	20·87	0·33	39·59	0·27	0·13	99·77	76·89
FMVDCT__F2	39·07	0·02	0·02	17·89	0·25	42·00	0·25	0·24	99·73	80·49
FMVDCT__G2	39·09	0·01	0·05	18·15	0·27	41·72	0·24	0·20	99·72	80·16
FMVDCT__H2	39·11	0·02	0·04	18·51	0·28	41·52	0·25	0·19	99·92	79·75
FMVDCT__I2	38·40	0·02	0·03	20·92	0·30	39·41	0·29	0·05	99·41	76·80
FMVDCT__J2	39·28	0·02	0·03	17·22	0·27	42·62	0·26	0·24	99·94	81·28
FMVDCT__A3a	39·06	0·02	0·04	18·45	0·27	41·34	0·26	0·13	99·56	79·74
FMVDCT__B3	39·40	0·01	0·06	16·77	0·26	42·85	0·26	0·23	99·84	81·78
FMVDCT__C3	38·31	0·03	0·03	22·33	0·35	38·23	0·28	0·07	99·63	75·02
FMVDCT__D3	38·92	0·03	0·03	19·34	0·30	40·63	0·27	0·13	99·65	78·66
FMVDCT__E3	38·55	0·01	0·03	21·53	0·29	38·75	0·30	0·05	99·50	76·00
FMVDCT__F3	39·71	0·01	0·04	13·67	0·19	45·42	0·22	0·42	99·69	85·38
FMVDCT__G3	38·37	0·02	0·02	21·52	0·38	39·05	0·27	0·16	99·78	76·07
FMVDCT__H3	39·20	0·03	0·06	17·91	0·27	41·83	0·18	0·17	99·66	80·40
FMVDCT__I3	38·97	0·03	0·04	18·56	0·30	41·45	0·29	0·18	99·82	79·67
FMVDCT__J3	39·26	0·04	0·06	18·20	0·28	41·79	0·27	0·16	100·06	80·13
FMVDCT__A4a	39·60	0·02	0·03	14·98	0·21	44·35	0·24	0·28	99·70	83·88
FMVDCT__B4	39·21	0·02	0·03	18·22	0·26	41·74	0·26	0·15	99·89	80·11
FMVDCT__C4	38·99	0·03	0·03	18·34	0·28	41·59	0·27	0·10	99·64	79·92
FMVDCT__D4	39·35	0·03	0·04	17·00	0·26	42·67	0·25	0·17	99·77	81·50
FMVDCT__E4	39·74	0·01	0·06	13·89	0·22	45·11	0·24	0·30	99·57	85·08
FMVDCT__F4	39·49	0·01	0·04	14·57	0·20	44·50	0·20	0·26	99·27	84·31
FMVDCT__G4	39·19	0·02	0·03	17·77	0·27	41·91	0·27	0·18	99·65	80·55
FMVDCT__I4	39·22	0·02	0·03	17·25	0·28	42·73	0·26	0·22	100·02	81·29
FMVDCT__H4	39·12	0·01	0·03	18·12	0·27	41·75	0·27	0·14	99·71	80·19
FMVDCT__J4	38·86	0·02	0·03	18·92	0·29	41·06	0·28	0·14	99·59	79·21
FMVDCT__A5	38·41	0·02	0·03	21·66	0·35	39·02	0·28	0·10	99·89	75·96
FMVDCT__B5	40·02	0·01	0·05	12·35	0·18	46·23	0·22	0·42	99·48	86·81
FMVDCT__C5a	40·11	0·00	0·06	12·75	0·18	46·15	0·23	0·35	99·84	86·41
FMVDCT__D5	39·25	0·02	0·04	17·07	0·24	42·46	0·25	0·24	99·56	81·38
FMVDCT__E5	39·23	0·02	0·03	17·31	0·27	42·44	0·28	0·17	99·76	81·14
FMVDCT__F5a	39·26	0·02	0·03	17·04	0·30	42·68	0·25	0·17	99·76	81·43
FMVDCT__G5	39·78	0·01	0·07	13·91	0·19	44·95	0·23	0·31	99·45	85·03
FMVDCT__H5a	39·75	0·01	0·06	14·37	0·23	44·73	0·24	0·29	99·69	84·52
FMVDCT__I5	38·84	0·03	0·04	18·18	0·26	41·51	0·25	0·16	99·28	80·05
FMVDCT__J5	38·36	0·03	0·02	21·74	0·38	38·50	0·28	0·09	99·40	75·63
FMVDCT__A6	38·65	0·02	0·05	19·76	0·30	40·07	0·20	0·09	99·13	78·08
FMVDCT__B6	39·09	0·01	0·05	17·09	0·27	42·36	0·24	0·19	99·30	81·31

(continued)

Table A1: Continued

Crystal	Oxide (wt %)									Mg#
	SiO_2	TiO_2	Al_2O_3	FeO	MnO	MgO	CaO	NiO	Total	
FMVDCT__C6	39·16	0·02	0·04	16·16	0·25	42·87	0·25	0·21	98·95	82·32
FMVDCT__D6	38·50	0·03	0·02	19·63	0·31	40·14	0·27	0·13	99·02	78·21
FMVDCT__E6	38·23	0·02	0·00	21·59	0·34	38·44	0·26	0·08	98·97	75·76
FMVDCT__F6	39·78	0·03	0·04	14·52	0·20	44·67	0·21	0·31	99·75	84·40
FMVDCT__G6	38·38	0·04	0·02	20·53	0·32	39·54	0·26	0·12	99·21	77·17
FMVDCT__H6	38·96	0·02	0·04	18·10	0·28	41·58	0·27	0·13	99·38	80·13
FMVDCT__I6	39·02	0·02	0·04	17·55	0·26	42·31	0·27	0·22	99·68	80·89
FMVDCT__J6	39·37	0·01	0·04	18·50	0·30	41·38	0·26	0·11	99·97	79·69
FMVDCT__A7	38·32	0·02	0·02	22·11	0·34	38·88	0·26	0·05	100·01	75·53
FMVDCT__B7a	38·85	0·04	0·03	19·36	0·34	40·55	0·25	0·17	99·59	78·58
FMVDCT__C7	38·63	0·02	0·02	20·95	0·30	39·54	0·28	0·13	99·86	76·84
FMVDCT__D7	38·81	0·03	0·03	18·99	0·28	41·16	0·26	0·14	99·69	79·20
FMVDCT__E7	40·05	0·02	0·06	13·45	0·19	45·78	0·25	0·37	100·16	85·68
FMVDCT__F7	38·81	0·02	0·02	20·15	0·32	40·10	0·27	0·17	99·85	77·74
FMVDCT__G7	40·26	0·02	0·05	11·86	0·18	46·72	0·23	0·34	99·64	87·37
FMVDCT__H7	38·86	0·03	0·04	19·70	0·30	40·30	0·28	0·11	99·61	78·22
FMVDCT__I7	39·10	0·00	0·05	18·18	0·26	41·79	0·25	0·15	99·78	80·16
FMVDCT__J7	39·37	0·01	0·06	16·06	0·21	43·77	0·23	0·23	99·94	82·74
FMVDCT__A8	38·68	0·03	0·04	20·25	0·28	40·19	0·28	0·15	99·88	77·73
FMVDCT__B8	39·49	0·02	0·04	17·44	0·26	42·50	0·25	0·26	100·26	81·06
FMVDCT__C8	39·13	0·02	0·03	18·34	0·27	41·77	0·28	0·10	99·95	80·00
FMVDCT__D8	39·28	0·02	0·05	17·12	0·27	42·63	0·25	0·19	99·80	81·38
FMVDCT__E8	38·93	0·04	0·04	19·37	0·28	40·70	0·28	0·11	99·77	78·69
FMVDCT__F8	39·31	0·03	0·03	17·00	0·28	42·99	0·25	0·18	100·06	81·60
FMVDCT__G8	39·08	0·03	0·03	18·32	0·28	41·61	0·27	0·17	99·79	79·95
FMVDCT__H8	38·75	0·02	0·02	19·70	0·30	40·67	0·28	0·12	99·86	78·38
FMVDCT__I8	39·44	0·02	0·04	15·97	0·22	43·37	0·26	0·22	99·54	82·69
FMVDCT__J8	39·60	0·00	0·04	14·47	0·19	44·69	0·24	0·33	99·55	84·46
FMVDCT__A9	39·52	0·01	0·05	14·61	0·20	44·74	0·24	0·30	99·67	84·34
FMVDCT__B9	39·27	0·01	0·03	16·57	0·25	43·20	0·25	0·23	99·81	82·07
FMVDCT__C9	39·05	0·01	0·04	17·72	0·27	42·16	0·26	0·20	99·73	80·69
FMVDCT__D9	39·20	0·02	0·05	17·19	0·25	42·57	0·21	0·19	99·69	81·31
FMVDCT__E9	39·50	0·02	0·04	16·90	0·23	42·84	0·22	0·23	99·99	81·68
FMVDCT__F9	38·30	0·02	0·03	21·07	0·31	39·00	0·28	0·09	99·10	76·48
FMVDCT__G9	38·78	0·03	0·03	20·92	0·28	39·50	0·30	0·03	99·86	76·85
FMVDCT__H9	39·21	0·02	0·02	16·99	0·28	42·51	0·26	0·21	99·50	81·44
FMVDCT__I9	39·18	0·02	0·04	16·94	0·24	42·62	0·23	0·23	99·49	81·56
FMVDCT__J9	39·78	0·01	0·05	13·64	0·19	45·22	0·24	0·29	99·42	85·35
FMVDCT__A10	39·70	0·02	0·05	14·19	0·17	44·85	0·23	0·32	99·52	84·77
FMVDCT__B10	38·94	0·02	0·05	18·76	0·27	41·56	0·21	0·19	100·01	79·56
FMVDCT__C10	39·36	0·01	0·05	18·65	0·26	41·76	0·23	0·12	100·43	79·75
FMVDCT__D10	39·20	0·03	0·04	18·01	0·27	41·82	0·26	0·19	99·82	80·31
FMVDCT__E10	39·02	0·03	0·05	18·13	0·24	41·67	0·24	0·22	99·60	80·17
FMVDCT__F10	39·28	0·03	0·02	16·13	0·23	43·45	0·26	0·28	99·69	82·56
FMVDCT__G10	38·55	0·01	0·02	20·82	0·32	39·59	0·29	0·10	99·71	76·95
FMVDCT__H10	39·07	0·01	0·06	18·12	0·26	41·75	0·23	0·15	99·64	80·20
FMVDCT__I10	39·42	0·01	0·05	16·06	0·25	43·38	0·27	0·30	99·74	82·58
FMVDCT__J10	38·41	0·03	0·03	22·20	0·36	38·42	0·24	0·04	99·74	75·22

Electron probe microanalysis data for 100 olivine crystal cores from a sample of Fimmvörðuháls tephra, erupted in 2010. Crystals were mounted in resin on a 10×10 grid, labelled A–J, 1–10. A 15 kV beam at 30 nA was used. Elemental abundances were measured against known standards using peak (P) and background (B) counting times as follows: Si P = 20 s, B = 10 s; Ni P = 50 s, B = 25 s; Fe P = 30 s, B = 15 s; Mn P = 10 s, B = 5 s; Al P = 60 s, B = 30 s; Ca P = 50 s, B = 25 s; Ti P = 20 s, B = 10 s; Mg P = 20 s, B = 10 s. Mg# = 100 Mg/[Mg + Fe(t) + Mn]. Internal standards used were olivine and hematite.

Table A2: XMT averaged grey-scale values of crystal core spots

Crystal	Average greyscale value
1	22036·62
2	22240·40
3	22304·52
4	22318·63
5	22332·52
6	22386·92
7	22386·94
8	22411·09
9	22428·06
10	22497·01
11	22500·18
12	22532·20
13	22563·31
14	22599·51
15	22644·19
16	22680·95
17	22693·69
18	22701·87
19	22717·55
20	22755·27
21	22755·69
22	22762·92
23	22770·07
24	22770·12
25	22791·85
26	22803·65
27	22826·04
28	22867·06
29	22872·01
30	22879·71
31	22886·65
32	22889·91
33	22897·38
34	22898·13
35	22902·99
36	22919·73
37	22920·37
38	22927·86
39	22943·27
40	22956·69
41	22964·50
42	22970·34
43	22971·84
44	22977·42
45	22982·00
46	22985·00
47	23000·41
48	23002·69
49	23002·72
50	23007·99
51	23012·22
52	23013·74
53	23017·99
54	23038·58
55	23047·08
56	23052·95
57	23063·83
58	23069·55
59	23069·61
60	23069·73
61	23089·71
62	23089·94
63	23107·06
64	23127·45
65	23132·32
66	23133·42
67	23136·40
68	23149·36
69	23152·86
70	23173·85
71	23183·52
72	23210·50
73	23211·85
74	23212·57
75	23217·59
76	23230·23
77	23254·65
78	23260·12
79	23310·84
80	23425·39
81	23444·72
82	23456·44
83	23467·67
84	23475·56
85	23476·79
86	23494·71
87	23518·67

X-ray micro-computed tomography data from the spots placed on 87 olivine crystal cores from a sample of Fimmvörðuháls tephra, erupted in 2010, calculated using the workflow detailed in the text and summarized in Fig. 2. Each spot is approximately 25 μm in diameter and 1 voxel deep.

Table A3: Rank-order and linear-array order of EPMA and XMT data

EPMA data				XMT data			
Mg#	Rank	Linear range	Differential*	Average greyscale value	Rank	Linear range	Differential*
75·02	100	75·02	0·00	22036·62	87	22037	0
75·22	99	75·15	0·07	22240·40	86	22054	−187
75·53	98	75·27	0·26	22304·52	85	22071	−233
75·63	97	75·40	0·23	22318·63	84	22088	−230
75·76	96	75·52	0·23	22332·52	83	22106	−227
75·96	95	75·65	0·31	22386·92	82	22123	−264
76·00	94	75·77	0·23	22386·94	81	22140	−247
76·07	93	75·90	0·17	22411·09	80	22157	−254
76·25	92	76·02	0·23	22428·06	79	22174	−254
76·48	91	76·15	0·33	22497·01	78	22192	−305
76·79	90	76·27	0·51	22500·18	77	22209	−291
76·80	89	76·40	0·40	22532·20	76	22226	−306
76·84	88	76·52	0·32	22563·31	75	22243	−320
76·85	87	76·64	0·21	22599·51	74	22261	−339
76·89	86	76·77	0·12	22644·19	73	22278	−366
76·95	85	76·89	0·06	22680·95	72	22295	−386
77·17	84	77·02	0·15	22693·69	71	22312	−381
77·23	83	77·14	0·09	22701·87	70	22330	−372
77·73	82	77·27	0·46	22717·55	69	22347	−371
77·74	81	77·39	0·35	22755·27	68	22364	−391
78·08	80	77·52	0·56	22755·69	67	22381	−374
78·21	79	77·64	0·56	22762·92	66	22399	−364
78·22	78	77·77	0·45	22770·07	65	22416	−354
78·31	77	77·89	0·42	22770·12	64	22433	−337
78·38	76	78·02	0·36	22791·85	63	22450	−342
78·58	75	78·14	0·44	22803·65	62	22467	−336
78·61	74	78·27	0·34	22826·04	61	22485	−341
78·66	73	78·39	0·27	22867·06	60	22502	−365
78·69	72	78·52	0·17	22872·01	59	22519	−353
78·77	71	78·64	0·13	22879·71	58	22536	−343
79·20	70	78·77	0·44	22886·65	57	22554	−333
79·21	69	78·89	0·32	22889·91	56	22571	−319
79·43	68	79·01	0·42	22897·38	55	22588	−309
79·56	67	79·14	0·42	22898·13	54	22605	−293
79·67	66	79·26	0·41	22902·99	53	22623	−280
79·69	65	79·39	0·30	22919·73	52	22640	−280
79·74	64	79·51	0·23	22920·37	51	22657	−263
79·75	63	79·64	0·11	22927·86	50	22674	−254
79·75	62	79·76	−0·02	22943·27	49	22691	−252
79·92	61	79·89	0·04	22956·69	48	22709	−248
79·95	60	80·01	−0·06	22964·50	47	22726	−239
80·00	59	80·14	−0·14	22970·34	46	22743	−227
80·05	58	80·26	−0·21	22971·84	45	22760	−211
80·11	57	80·39	−0·28	22977·42	44	22778	−200
80·13	56	80·51	−0·39	22982·00	43	22795	−187

(continued)

Table A3: Continued

EPMA data				XMT data			
Mg#	Rank	Linear range	Differential*	Average greyscale value	Rank	Linear range	Differential*
80·13	55	80·64	−0·51	22985·00	42	22812	−173
80·16	54	80·76	−0·60	23000·41	41	22829	−171
80·16	53	80·89	−0·73	23002·69	40	22847	−156
80·17	52	81·01	−0·84	23002·72	39	22864	−139
80·19	51	81·13	−0·95	23007·99	38	22881	−127
80·20	50	81·26	−1·06	23012·22	37	22898	−114
80·31	49	81·38	−1·08	23013·74	36	22916	−98
80·40	48	81·51	−1·11	23017·99	35	22933	−85
80·49	47	81·63	−1·15	23038·58	34	22950	−89
80·55	46	81·76	−1·21	23047·08	33	22967	−80
80·69	45	81·88	−1·20	23052·95	32	22984	−69
80·89	44	82·01	−1·11	23063·83	31	23002	−62
81·06	43	82·13	−1·07	23069·55	30	23019	−51
81·14	42	82·26	−1·12	23069·61	29	23036	−33
81·28	41	82·38	−1·10	23069·73	28	23053	−16
81·29	40	82·51	−1·21	23089·71	27	23071	−19
81·31	39	82·63	−1·32	23089·94	26	23088	−2
81·31	38	82·76	−1·44	23107·06	25	23105	−2
81·38	37	82·88	−1·50	23127·45	24	23122	−5
81·38	36	83·01	−1·62	23132·32	23	23140	7
81·43	35	83·13	−1·70	23133·42	22	23157	23
81·44	34	83·25	−1·82	23136·40	21	23174	38
81·50	33	83·38	−1·88	23149·36	20	23191	42
81·56	32	83·50	−1·95	23152·86	19	23208	56
81·60	31	83·63	−2·03	23173·85	18	23226	52
81·68	30	83·75	−2·08	23183·52	17	23243	59
81·78	29	83·88	−2·10	23210·50	16	23260	50
81·90	28	84·00	−2·11	23211·85	15	23277	66
82·07	27	84·13	−2·06	23212·57	14	23295	82
82·32	26	84·25	−1·93	23217·59	13	23312	94
82·56	25	84·38	−1·82	23230·23	12	23329	99
82·58	24	84·50	−1·92	23254·65	11	23346	92
82·59	23	84·63	−2·04	23260·12	10	23364	103
82·69	22	84·75	−2·07	23310·84	9	23381	70
82·74	21	84·88	−2·13	23425·39	8	23398	−27
83·56	20	85·00	−1·44	23444·72	7	23415	−29
83·88	19	85·13	−1·24	23456·44	6	23433	−24
84·31	18	85·25	−0·94	23467·67	5	23450	−18
84·34	17	85·38	−1·03	23475·56	4	23467	−9
84·37	16	85·50	−1·13	23476·79	3	23484	7
84·40	15	85·62	−1·22	23494·71	2	23501	7
84·46	14	85·75	−1·29	23518·67	1	23519	0
84·52	13	85·87	−1·35				
84·77	12	86·00	−1·23				
84·83	11	86·12	−1·29				

(continued)

Table A3: Continued

EPMA data				XMT data			
Mg#	Rank	Linear range	Differential*	Average greyscale value	Rank	Linear range	Differential*
85·03	10	86·25	−1·22				
85·08	9	86·37	−1·30				
85·17	8	86·50	−1·33				
85·35	7	86·62	−1·27				
85·38	6	86·75	−1·37				
85·68	5	86·87	−1·19				
86·41	4	87·00	−0·58				
86·81	3	87·12	−0·31				
87·10	2	87·25	−0·14				
87·37	1	87·37	0·00				

Rank-order and linear-array-order data used to generate plots displayed in Fig. A1. It should be noted that higher greyscale values denote lighter voxels = lower Mg#. The XMT linear-array order is inverted to allow comparison against Mg#. Four significant figures are retained when describing EPMA data, to maintain unique numbers and illustrate the shape of the arrays.
*The differential captures the degree to which each data point (each crystal) departs from a straight line between the highest and lowest value on the corresponding rank-order plot, so that comparisons are easier to make visually (see Fig. A1).

Table A4: Bins used to generate frequency diagram from XMT greyscale spots

Bin no.	Range	
	from	to
1	23550	+
2	23378	23550
3	23206	23378
4	23033	23206
5	22861	23033
6	22689	22861
7	22517	22689
8	22344	22517
9	22172	22344
10	22000	22172
11	-	22000